AIAA SciTech Forum
8-12 January 2024, Orlando, FL
AIAA SCITECH 2024 Forum

10.2514/6.2024-1082

Utilizing a retrospective cost adaptation (RCA) algorithm to achieve data-driven, adaptive, real-time (DART) precision meteorological forecasts

Sujit Sinha *, Rui Fu †, Sean Bailey ‡, Jesse B. Hoagg §, and Alexandre Martin ¶
University of Kentucky, Lexington, Kentucky, 40506

Highly-localized weather forecasts are an emerging need for the operational flight safety of uncrewed aerial vehicles (UAVs), particularly given the expected growth of UAV shipments and uses. Highly-localized forecasts will also serve to improve the tracking of toxic or contaminant clouds associated with accidents or incidents such as a train derailment or chemical plant fire. Therefore, with the ultimate goal of creating a data-driven, adaptive, real-time (DART) solution, the Weather Research and Forecasting (WRF) model has been augmented with a retrospective cost adaptation (RCA) algorithm as a potential means for improving precision meteorological (sub-1 km) forecasts. The RCA algorithm serves to adapt the simulated horizontal wind speed component values to observed measurements collected by appropriately instrumented UAVs at specified geographic locations. Horizontal wind speed data that was incidentally gathered from a UAV formation flight control experiment at the University of Kentucky flight field was employed to evaluate and validate the DART solution. The results indicate that when the RCA algorithm is employed with the WRF model, there is a 14% reduction in both the u and v wind speed component mean absolute errors compared to the baseline WRF model. The next step is to further validate the WRF model augmented with the RCA algorithm via flight test data collected specifically for this purpose in August 2023 at the University of Kentucky flight field. Once the promise of the DART approach is fully proven and operational, the ensuing forecasts will benefit the UAV community and contaminant incident first responders.

Nomenclature

Weather Research & Forecasting (WRF) Model

η	=	traditional terrain-following hydrostatic vertical coordinate system
η_c	=	user-specified value of η where vertical coordinate fully transitions to pressure-based
p_d	=	pressure of dry air
p_t	=	pressure at selected atmospheric top
p_s	=	pressure at surface
β	=	third order polynomial to transition from sigma vertical coordinate to a pressure based vertical coordinate
c_1, c_2, c_3, c_4	=	coefficients of third order polynomial
μ_d	=	vertical coordinate
g	=	gravitational acceleration
ρ_d	=	density of air
Δz	=	vertical height
$\mathbf{V}$	=	velocity vector
$\mathbf{v}$	=	covariant velocity vector
ω	=	contravariant vertical velocity
θ_m	=	moist potential temperature
q_m	=	mixing ratios of moisture variables

*Graduate Research Assistant, Mechanical and Aerospace Engineering, AIAA Student Member.
†Research Scientist, Mechanical and Aerospace Engineering, AIAA Member.
‡Professor, Mechanical and Aerospace Engineering, Associate Fellow AIAA.
§Professor and Chair, Mechanical and Aerospace Mechanical and Aerospace Engineering.
¶Professor, Mechanical and Aerospace Engineering, Associate Fellow AIAA.

ϕ	=	geopotential
α	=	inverse of density for air
α_d	=	inverse of density for dry air
U, V	=	horizontal velocity components
W	=	vertical velocity component
γ	=	specific heat ratio for dry air
R_d	=	ideal gas constant for dry air
p_0	=	reference surface pressure (typically 10^5 pascals)
F_U, F_V, F_W, F_Θ	=	forcing terms as a result of physics, turbulent mixing, spherical projections, and earth's rotation models
t	=	time
F_X, F_Y	=	independent forcing terms used by RCA algorithm as the adaptation parameter $\theta(n)$

Retrospective Cost Adaptation (RCA) Algorithm

Δt_{adapt}	=	adaptation time step
η_{adapt}	=	positive integer
Δt	=	computation time step
N	=	number of measurement locations
n	=	adaptation time step
$\theta(n)$	=	parameter modified to adapt simulation to measurements
$\phi_{m,i}$	=	measurement at the i^{th} location
$\phi_{s,i}$	=	simulated value at the i^{th} location
$\zeta(n)$	=	performance, difference between simulated and measured values at specified locations
f	=	feedback vector of simulated results
$M_i(n)$	=	set of square matrices $(\theta \times \theta)$ at each adaptation time step
$N_i(n)$	=	set of matrices $(\theta \times f)$ at each adaptation time step
$L(n)$	=	set of column matrices $(1 \times \theta)$ at each adaptation time step
Q	=	adaptive parameter
ψ	=	column matrix composed of the feedback vector, $\theta(n)$, and value 1
$\hat{Q}$	=	optimization variable
ζ_r	=	retrospective performance
H_j	=	jth impulse response parameter from θ to ζ
q	=	stacked matrix of adaptive parameter Q
$\hat{q}$	=	stacked matrix of optimization variable $\hat{Q}$
J	=	retrospective cost

RCA Subscripts

m	=	measurement
s	=	simulated
r	=	retrospective

I. Introduction

Given the anticipated growth of the commercial UAV market, there is a growing need for data-driven, adaptive, real-time (DART) precision meteorological (sub 1-km forecasts) for two reasons: 1) to boost public safety by tracking hazardous contaminant clouds to better inform evacuation decisions; and 2) to improve unmanned aerial vehicle (UAV) flight safety by avoiding hazardous flight regimes.

II. Operational Concept

The operational concept for improving precision meteorological forecasts is effectively the same as that for tracking a contaminant cloud, which is depicted in Fig. 1. At the location of a contaminant dispersion or the atmospheric/geographic area of interest, a swarm of UAVs outfitted with appropriate sensors will be deployed. By flying in an autonomous or semi-autonomous pattern, the UAVs will collect meteorological information and toxic particulate information, in the case of tracking a contaminant cloud, that is telemetered in real-time to a mobile ground station. A numerical weather

prediction (NWP) model immediately assimilates the data and is executed to provide a near-real-time forecast. Although the figure depicts that the model is hosted at a central data center, ultimately, the concept is to house the NWP model on a deployable server in a motor vehicle such as a van. Next, the forecast is telemetered up to the swarm's guidance system, which uses the information to reposition the UAVs to collect the next most beneficial set of observations. The process is then cyclically repeated such that new observations are continuously telemetered to the ground station, assimilated into the weather model, and then the revised forecast is telemetered back to the swarm's guidance system to reposition the UAVs. So, in summary, the operational concept employs a UAV-based measurement system to develop a data-driven, adaptive, real-time (DART) meteorological forecast update within a small geographic region.

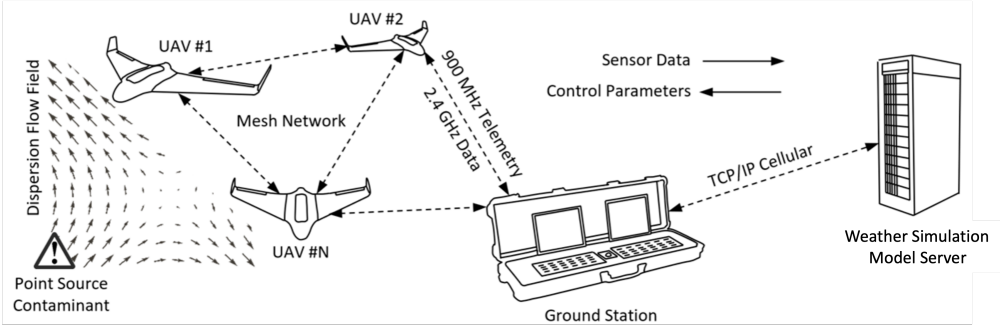

Fig. 1 DART operational diagram for tracking a contaminant cloud

A. Use Cases

Firstly, the projected use in a wide range of industries and applications is driving growth in the commercial global UAV market from USD 10.98 billion in 2022 to USD 54.81 billion in 2030 [1]. Currently, photography is the dominant drone use case, followed by agriculture and inspection associated with real estate [2]. However, the future growth of the UAV market will be increasingly due to emerging uses such as disaster management, relief and rescue operations, and logistics and transportation operations [2]. Additionally, over the next ten years, the use cases involving distribution and transportation will have the largest economic impact [3].

Regarding the UAV military market, a report by Fortune Business Insight estimates that by 2030, the worldwide market size is expected to grow from USD 12.55 billion to USD 35.60 billions [4]. Therefore, the size of the military market is anticipated to grow at a slower rate, even though it is currently larger than the commercial market. Drones employed by the military are utilized for both tactical and strategic purposes, including supply logistics, combat sorties, reconnaissance, and surveillance [5].

Given the foreseen growth in both the commercial and military UAV markets, precision weather forecasts will be an imperative to maximize UAV asset utilization while minimizing operational flight risk.

Secondly, given the worldwide trend of increased urbanization, any transportation mishap that releases dust, debris, or toxins into the atmosphere has the potential to endanger nearby inhabitants. An analysis of the U.S. DOT Pipeline and Hazardous Materials Safety Administration database [6] indicates that there are about 280 'vapor(gas) dispersion' occurrences in the United States each year. The damages resulting from these dispersions are not in direct proportion to the number of incidences and range from USD 2 million to USD 31 million between 2014 and 2022. Consequently, regardless of the cause, improving the capability to track dispersions via improved precision meteorological predictions will benefit first responders in public evacuation decision-making.

B. Prior Research

The history of weather forecasting is quite lengthy and started well before 1848, when the Smithsonian launched a meteorological observation program that sought to leverage the newly implemented telegraph networks to provide advance notice of bad weather [7]. More recently, precision weather modeling progress has been made by studies examining high-resolution planetary boundary layer (PBL) forecasts. A dissertation by Mayer (2011) [8] provided a synthesis and collection of papers covering the use of a UAV for PBL studies, while a technical report by Passner et al. (2012) [9] evaluated real-time weather observations from a UAV to update the Weather Research and Forecast (WRF) model with observation nudging. Papers by Jacob et al. (2018) [10] and Nolan et al. (2018)[11] employed large eddy

simulation (LES) models to profile the boundary layer by representing the flight of small UAVs and predict Lagrangian coherent structures, which can contain concentrations of hazardous gas, respectively. In addition, studies by Liu et al. (2020) [12] and a dissertation by Wiersema (2020) [13] have used the WRF-LES model with fine grid resolutions to study regions with complex terrain, like mountainous areas. Some studies have evaluated the dynamic downscaling of WRF model predictions, such as [14]. Moreover, Abdelghaffar et al. (2017) [15] have looked at contaminant source localization techniques to feed UAV decision-making algorithms as a way to identify the location of the next observation sample. Furthermore, the WRF-LES model was employed in a paper by Pinto et al. (2021) [16] to support real-time flight planning, while the FastEddy® model was used by Muñoz-Esparza et al. (2021) [17] to explore micro-scale weather modeling to support UAV operations in an urban environment.

C. Study Scope

This study seeks to build on the aforementioned prior efforts by taking an initial step towards a DART weather simulation model by developing a data-driven, adaptive model while bearing in mind the real-time requirement. Consequently, two major components are required: 1) a numerical weather model on the front end; and 2) a real-time, or near-real-time, method to adapt the model to observations on the back end. So, as depicted in the middle box in Fig. 2, the research scope is to augment the Weather Research and Forecasting (WRF) model with the retrospective cost adaptation (RCA) algorithm.

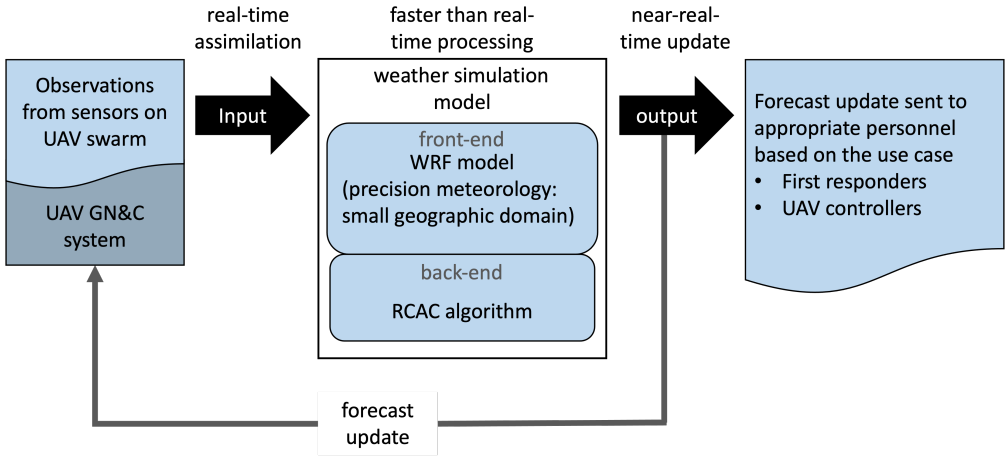

Fig. 2 Research scope is to develop a DART solution utilizing the WRF model augmented with the RCA algorithm

The WRF model, or more specifically, the Advanced Research WRF (ARW) model, is open-source code that is managed by the University Center for Atmospheric Research (UCAR) for the National Center of Atmospheric Research (NCAR). An overview of this model is provided in the next subsection, while the governing equations are described in the Numerical Frameworks and Formulations section.

The RCA algorithm was originally developed in the adaptive control literature. Additional information about the history of this algorithm and the algorithm formulation as applied in this research is also provided in the Numerical Frameworks and Formulations section.

D. Weather Research and Forecast (WRF) Model

1. Overview

The selected NWP model for this effort is the Weather Research and Forecasting (WRF) model, or more specifically, the Advanced Research WRF (ARW) model, which is managed by the University Center for Atmospheric Research (UCAR) for the National Center of Atmospheric Research (NCAR). Briefly stated, the ARW model solves the conservation of mass, momentum, and energy equations along with the equation of state (ideal gas law), with a hybrid-terrain-following hydrostatic-pressure vertical coordinate system, various physics options — microphysics, cumulus parameterizations, surface physics, planetary boundary layer physics, and atmospheric radiation physics —

and employs a time-split Runge-Kutta integration scheme [18, 19]. The major elements or programs of the WRF model are [18]:

- **WRF Preprocessing System (WPS)**: Synthesizes observations from various meteorological stations and sources for input into real.exe
- **WRFDA (WRF Data Assimilation)**: Data assimilation program for updating the simulation with real-time observations
- **Advanced Research WRF (ARW)**: Global weather simulation, which generates the model forecast
- **Post-processing/Visualization Tools**: Graphic, plotting, and animating results

The governing equations in this model are presented in the next section, Numerical Framework and Formulations.

2. WRF Large Eddy Simulation (WRF-LES)

For cases where the horizontal grid resolution is 1-km or greater, twelve user-selected atmospheric boundary layer (ABL) or planetary boundary layer (PBL) schemes are available, as listed in the WRF V4 Description [19]. However, WRF has the option to run a large eddy simulation (LES) at high resolutions to capture small-scale phenomena and is commonly referred to as WRF-LES. Given that the use cases are for precision meteorology within the PBL, the LES option of WRF was employed for all simulations. The resolution for the WRF-LES is much finer but is constrained near the surface to a maximum vertical resolution of 16 meters and a maximum horizontal resolution of 30 meters, due to the heterogeneous surface and elevation [20]. Moreover, data assimilation is also possible with WRF-LES and is referred to as WRF real-time four-dimensional data assimilation LES (WRF RTFDDA-LES) [21]. In LES mode, large turbulent eddies are explicitly resolved, although turbulence that is below the filter imposed by the computational grid must still be determined via a sub-grid scale (SGS) model [22]. The choices of these models include a constant scheme, a 1.5-order prognostic equation for turbulent kinetic energy (TKE) scheme, a 3D Smagorinsky first-order turbulence closure scheme, and a 2D Smagorinsky scheme based only on horizontal wind for horizontal diffusion [18, 19]. Note that the TKE model was utilized for all simulations performed in this study.

III. Numerical Framework and Formulations

A. WRF Governing Equations

Please note that the governing equations as described below are per the NCAR Technical Note, *A Description of the Advanced Research WRF Version 4* [19]. This information is included herein for completeness.

A traditional terrain-following hydrostatic pressure vertical coordinate system, or mass vertical coordinate, is given by [23]

$$\eta = \frac{p_d - p_t}{p_s - p_t} \tag{1}$$

where the hydrostatic component of the pressure of dry air is p_d, while the pressure at the top and surface boundaries are represented by p_t and p_s, respectively. Note that while terrain-following hydrostatic pressure coordinates are commonly described as “sigma" coordinates, in the case of the WRF model, the sigma coordinate employs the Greek letter eta.

Version 4 of the WRF ARW has changed this traditional sigma coordinate to a hybrid coordinate, as defined by Park (2003) [24], that permits the terrain effects to be ramped out with increasing altitude. A third-order polynomial, which allows for a means to smooth the transition from a sigma coordinate at the surface to purely a pressure coordinate at upper levels, is established as

$$B(\eta) = c_1 + c_2\eta + c_3\eta^2 + c_4\eta^3 \tag{2}$$

subject to the following boundary conditions (where the subscript η indicates differentiation),

$$B(1) = 1, \quad B_\eta(1) = 1, \quad B(\eta_c) = 0 \quad B_\eta(\eta_c) = 0, \tag{3}$$

yielding,

$$c_1 = \frac{2\eta_c^2}{(1-\eta_c)^3}, \quad c_2 = \frac{-\eta_c(4+\eta_c+\eta_c^2)}{(1-\eta_c)^3}, \quad c_3 = \frac{2(1+\eta_c+\eta_c^2)}{(1-\eta_c)^3}, \quad c_4 = \frac{-(1+\eta_c)}{(1-\eta_c)^3}, \tag{4}$$

noting that η_c is user-specified value of η where the vertical coordinate fully transitions to purely a pressure method.

The vertical coordinate is thereby defined by

$$\mu_d = \frac{\partial p_d}{\partial \eta} = B_\eta(\eta)(p_s - p_t) + [1 - B_\eta(\eta)](p_0 - p_t) \tag{5}$$

Given that within a grid cell, $\mu_d \Delta\eta = \Delta p_d = -g\rho\Delta z$ is proportional to the mass per unit area, the flux form of the prognostic variables is given by

$$\mathbf{V} = \mu_d \mathbf{v} = (U, V, W), \qquad \Omega = \mu_d \omega, \qquad \Theta_m = \mu_d \theta_m, \qquad Q_m = \mu_d q_m, \tag{6}$$

where, $\mathbf{v} = (u, v, w)$ are the horizontal and vertical direction covariant velocities, and $\omega = \dot{\eta}$ is the contravariant 'vertical' velocity. In addition, the moist potential temperature is given by $\theta_m = \theta(1 + (R_v/R_d)q_v) \approx \theta(1 + 1.61 q_v)$, while the mixing ratios of moisture variables -- water vapor, cloud water, rain, water, etc., -- is given by $Q_m = \mu_d q_m$, where $q_m = q_v, q_c, q_r$, etc.

The governing equations of the ARW model also include the non-conserved variables, specifically the geopotential ($\phi = gz$), even though this parameter is a prognostic variable, pressure (p), the inverse density of dry air ($\alpha_d = 1/\rho_d$), and the inverse density taking into account the full parcel density $\alpha = \alpha_d(1 + q_v + q_c + q_r + q_i + ...)^{-1}$

Therefore, by employing the variables defined above, the Euler equations in flux form are:

$$\frac{\partial U}{\partial t} + (\nabla \cdot \mathbf{V}u) + \mu_d \alpha \frac{\partial p}{\partial x} + \left(\frac{\alpha}{\alpha_d}\right)\frac{\partial p}{\partial \eta}\frac{\partial \phi}{\partial x} = F_U \tag{7}$$

$$\frac{\partial V}{\partial t} + (\nabla \cdot \mathbf{V}v) + \mu_d \alpha \frac{\partial p}{\partial y} + \left(\frac{\alpha}{\alpha_d}\right)\frac{\partial p}{\partial \eta}\frac{\partial \phi}{\partial y} = F_V \tag{8}$$

$$\frac{\partial W}{\partial t} + (\nabla \cdot \mathbf{V}w) - \left[g\left(\frac{\alpha}{\alpha_d}\right)\frac{\partial p}{\partial \eta} - \mu_d\right] = F_W \tag{9}$$

$$\frac{\partial \Theta_m}{\partial t} + (\nabla \cdot \mathbf{V}\theta_m) = F_{\Theta_m} \tag{10}$$

$$\frac{\partial \mu_d}{\partial t} + (\nabla \cdot \mathbf{V}) = 0 \tag{11}$$

$$\frac{\partial \phi}{\partial t} + \mu^{-1}[(\mathbf{V} \cdot \nabla\phi) - gW] = 0 \tag{12}$$

$$\frac{\partial Q_m}{\partial t} + (\nabla \cdot \mathbf{V}q_m) = F_{Q_m} \tag{13}$$

plus the diagnostic relation for the dry hydrostatic pressure:

$$\frac{\partial \phi}{\partial \eta} = -\alpha_d \mu_d \tag{14}$$

along with the diagnostic relation for for the full pressure (dry air plus water vapor), which is the equation of state:

$$p = p_0 \left(\frac{R_d \theta_m}{p_0 \alpha_d}\right)^\gamma \tag{15}$$

Note that if a is employed to represent a generic variable, then:

$$\nabla \cdot \mathbf{V}a = \frac{\partial (Ua)}{\partial x} + \frac{\partial (Va)}{\partial y} + \frac{\partial (\Omega a)}{\partial \eta} \tag{16}$$

and

$$\mathbf{V} \cdot \nabla a = U\frac{\partial a}{\partial x} + V\frac{\partial a}{\partial y} + \Omega\frac{\partial a}{\partial \eta} \tag{17}$$

The specific heat ratio for dry air is $\gamma = c_p/c_v = 1.4$, the gas constant for dry air is represented by R_d, and a reference surface pressure is given by p_0, which is typically 10^5 pascals. Also, the terms F_U, F_V, F_W, and F_Θ on the right-hand side (RHS) are forcing terms that occur as a result of physics, turbulent mixing, spherical projections, and the earth's rotation models.

Eq. (7) through Eq. (15) are the basic governing equations in the ARW model; however, in reality, the equations are more complex. This complexity is due to recasting these governing equations to use perturbation variables as a means to reduce: 1) truncation errors in the horizontal pressure gradient calculations in the discrete solver; and 2) machine rounding errors in the vertical pressure gradient and buoyancy calculations. The details of these modifications are detailed in the ARW description technical note [19].

B. Retrospective cost adaptation algorithm

Firstly, please note that the description of the RCA algorithm presented in this section is derived from Li et al. (2017, 2018) [25, 26], Fu et al. (2022) [27], and Sinha et al. (2023) [28].

The RCA algorithm was originally developed in the adaptive control literature. Specifically, Venugopal (2000) [29] presents a gradient-based RCA algorithm that is effective for active noise control. A recursive-least-squares (RLS)-based RCA algorithm is presented in Hoagg (2010, 2012) [30, 31].

In Li et al. (2018) [26], the RLS-based RCA algorithm is adopted for data-driven model adaptation rather than adaptive control, where it was specifically used for data-driven model adaptation of the closure coefficients in a Reynolds-averaged Navier-Stokes k-ω model. Fu et al. (2022) [27] uses the RLS-based RCA to model material property behavior.

In this work, RLS-based RCA is used to adapt independent forcing terms added to the WRF governing horizontal momentum equations. Equations (7) and (8) are revised with an additional term each and written as

$$\frac{\partial U}{\partial t} + (\nabla \cdot \mathbf{V}u) + \mu_d \alpha \frac{\partial p}{\partial x} + \left(\frac{\alpha}{\alpha_d}\right)\frac{\partial p}{\partial \eta}\frac{\partial \phi}{\partial x} - F_U = F_X \tag{18}$$

$$\frac{\partial V}{\partial t} + (\nabla \cdot \mathbf{V}\upsilon) + \mu_d \alpha \frac{\partial p}{\partial y} + \left(\frac{\alpha}{\alpha_d}\right)\frac{\partial p}{\partial \eta}\frac{\partial \phi}{\partial y} - F_V = F_Y \tag{19}$$

where F_X and F_Y are independent forcing terms for the x and y directions, respectively. These terms are the ones that will be adapted by the RCA algorithm and notated as $\theta(n)$.

In addition, the first terms on the left-hand side of equations (18) and (19) are the temporal acceleration tendencies in the x and y directions, respectively, while the second terms are the advection tendencies. The third and fourth terms on the left-hand side of these equations represent the pressure gradient tendencies. In sum, these first four terms on the left-hand side of equations (18) and (19) are the total mass-coupled horizontal momentum non-physics tendencies for the x and y directions, respectively.

Furthermore, F_U and F_V are the net effects of forces in the x and y directions, respectively, due to Earth curvature, Coriolis, turbulent mixing, horizontal diffusion, vertical diffusion, and radiation. These terms are the total mass-coupled horizontal momentum physics tendencies.

With F_X and F_Y established as $\theta(n)$, the RCA algorithm is given by

$$\theta(n) = [F_X(n) \;\; F_Y(n)]^{\mathrm{T}} \in \mathbb{R}^{l_\theta}, \tag{20}$$

where $n \in \mathbb{N} \triangleq \{0, 1, 2, 3, \dots\}$ and n is the adaptation time step. The independent forcing terms $\theta(n)$ are updated with the time step $\Delta t_{\text{adapt}} \triangleq \eta_{\text{adapt}} \Delta t$, where η_{adapt} is a positive integer and Δt is the WRF integration time step. To achieve convergence of the RCA algorithm, η_{adapt} was set to a value of one, and therefore Δt_{adapt} was equivalent to Δt, meaning that one adaptation time step occurred with every iteration of the WRF model's 3rd order Runge-Kutta split-time step computations.

Next, measured values consisting of the x-component of wind speed magnitude (u) and the y-component of wind speed magnitude (υ), for a combined total of $2N$ measurements at N specified locations, are required for the RCA algorithm. Within the context of this algorithm, the term *measurement* is defined as *a priori* information about the horizontal velocity distribution at the N locations. The measurements and the associated simulated values are specified by

$$\Phi_m \triangleq \begin{bmatrix} \phi_{m,\,1}(n) \\ \vdots \\ \phi_{m,\,2N}(n) \end{bmatrix} \in \mathbb{R}^{l_\Phi}, \tag{21}$$

$$\Phi_s \triangleq \begin{bmatrix} \phi_{s,\,1}(n) \\ \vdots \\ \phi_{s,\,2N}(n) \end{bmatrix} \in \mathbb{R}^{l_\Phi}, \tag{22}$$

where $\phi_{m,i}(n) \in \mathbb{R}^{l_i}$ is the i^{th} measurement value, $\phi_{s,i}(n) \in \mathbb{R}^{l_i}$ is the i^{th} simulated value, $l_\Phi \triangleq \sum_{i=1}^{N} l_i$, and $n \in \mathbb{N}$, $i = 1, \ldots, 2N$, since each location has a u measured value and a v measured value. To adapt $\theta(n)$, *performance* is defined as

$$\zeta(n) \triangleq \Phi_s(n) - \Phi_m(n). \tag{23}$$

The external driver for $\theta(n)$ is a vector of simulated flow-field output (horizontal wind speed component magnitudes u and v for this study), which is denoted by $f(n) \in \mathbb{R}^{l_f}$. Then, for all $n \in \mathbb{N}$, θ_n is determined from an auto-regressive moving-average (ARMA) model with a feed-forward bias as given by

$$\theta(n) = \sum_{i=1}^{n_c} M_i(n)\theta(n-i) + \sum_{i=1}^{n_c} N_i(n) f(n-i) + L(n), \tag{24}$$

where n_c is a positive integer, $M_i(n) \in \mathbb{R}^{l_\theta \times l_\theta}$ is a square matrix at each adaptation time step, $N_i(n) \in \mathbb{R}^{l_\theta \times l_f}$ is a matrix at each adaptation time step, and $L(n) \in \mathbb{R}^{l_\theta}$ is a column at each adaptation time step.

Note that $M_i(n)$ is the auto-regressive parameter, $N_i(n)$ is the moving average, and $L(n)$ is the feed-forward bias, and these values are updated according to the adaptive law presented herein. The ARMA model is initialized with $M_i(0) = 0_{l_\theta \times l_\theta}$, $N_i(0) = 0_{l_\theta \times l_f}$, and $L(0) \in \mathbb{R}^{l_\theta}$ for the F_X and F_Y independent forcing terms. For this study, $L(0) = 0_{l_\theta}$, since an initial feed-forward bias is not applied. The ARMA model, Eq. (24), can be rewritten as

$$\theta(n) = Q(n)\psi(n), \tag{25}$$

where $Q(n)$ is the adaptive parameter given by

$$Q(n) = \begin{bmatrix} N_1(n) \cdots N_{n_c}(n) & M_1(n) \cdots M_{n_c}(n) & L(n) \end{bmatrix} \in \mathbb{R}^{l_\theta \times (n_c(l_f + l_\theta)+1)}, \tag{26}$$

and

$$\psi(n) \triangleq \begin{bmatrix} f(n-1) \\ \vdots \\ f(n-n_c) \\ \theta(n-1) \\ \vdots \\ \theta(n-n_c) \\ 1 \end{bmatrix} \in \mathbb{R}^{(n_c(l_f+l_\theta)+1)}. \tag{27}$$

Next, an update equation for $Q(n)$ is expressed by setting $\hat{Q}$ as the optimization variable and defining *retrospective performance* as

$$\hat{\zeta}_r(\hat{Q}, n) \triangleq \zeta(n) + \sum_{j=0}^{n_r} H_j \left[\hat{Q} - Q(n-j)\right]\psi(n-j), \tag{28}$$

where $\hat{Q} \in \mathbb{R}^{l_\theta \times (n_c(l_f+l_\theta)+1)}$ and $\hat{Q}$ is Q initially, n_r is a positive integer, $H_j \in \mathbb{R}^{l_\Phi \times l_\theta}$ is the j^{th} impulse-response parameter from θ to ζ. The methodology to determine H_j is available as described in [26], with additional detail provided in [27]. For this study, H_j was analytically calculated to be a diagonal matrix with a constant value on the diagonal equivalent to the WRF model Domain 3 integration time step size, although this diagonal constant value had to be increased to 2.6 in order to prevent the algorithm from becoming unstable.

The retrospective performance is calculated based on the true performance by assuming that the optimization variable $\hat{Q}$ was employed in place of prior adaptive parameters $Q(n), \ldots, Q(n-n_r)$. As a result, the retrospective performance serves as a proxy for the actual performance. The adaptive parameter is deemed to have converged when $Q(n)$ is constant, indicating that $Q(n-i) \equiv Q(n)$, in which case $\hat{\zeta}_r(Q(n), n) \equiv \zeta(n)$.

Recalling that vec X is the vector created by stacking the columns of matrix X, the following two stack matrices can be defined

$$q(n) \triangleq \text{vec}\, Q(n) \in \mathbb{R}^{l_q}, \tag{29}$$

$$\hat{q} \triangleq \operatorname{vec} \hat{Q} \in \mathbb{R}^{l_q}, \tag{30}$$

where $l_q \triangleq l_\theta(n_c(l_f + l_\theta) + 1)$. Therefore, retrospective performance can be rewritten as

$$\hat{\zeta}_r(\hat{q}, n) = \zeta(n) + \sum_{j=0}^{n_r} \left[\psi^{\mathrm{T}}(n-j) \otimes H_j\right] \hat{q} - \sum_{j=0}^{n_r} H_j \theta(n-j), \tag{31}$$

or

$$\hat{\zeta}_r(\hat{q}, n) = \zeta(n) + \Psi^{\mathrm{T}}(n)\hat{q} - \sum_{j=0}^{n_r} H_j \theta(n-j), \tag{32}$$

where $\otimes$ represents the Kronecker product, and

$$\Psi(n) \triangleq \sum_{j=0}^{n_r} \psi(n-j) \otimes H_j^{\mathrm{T}} \in \mathbb{R}^{l_q \times l_\Phi}. \tag{33}$$

Next, the retrospective cost is

$$J(\hat{q}, n) \triangleq \sum_{i=0}^{n} \hat{\zeta}_r^{\mathrm{T}}(\hat{q}, i)\hat{\zeta}_r(\hat{q}, i) + \left[\hat{q} - q(0)\right]^{\mathrm{T}} \Gamma \left[\hat{q} - q(0)\right]. \tag{34}$$

Note that $\Gamma \in \mathbb{R}^{l_q \times l_q}$ is symmetric and positive definite. The unique global minimizer of the retrospective cost J, for each $n \in \mathbb{N}$, is given by

$$q(n+1) = q(n) - P(n)\Psi(n)\Omega^{-1}(n)\zeta_r(n), \tag{35}$$

where

$$P(n+1) = P(n) - P(n)\Psi(n)\Omega^{-1}(n)\Psi^{\mathrm{T}}(n)P(n), \tag{36}$$

$$\zeta_r(n) \triangleq \hat{\zeta}_r(q(n), n) = \zeta(n) + \Psi^{\mathrm{T}}(n)q(n) - \sum_{j=0}^{n_r} H_j \theta(n-j), \tag{37}$$

$$\Omega(n) \triangleq I_{l_\Phi} + \Psi^{\mathrm{T}}(n)P(n)\Psi(n), \tag{38}$$

and $P(0) = \Gamma^{-1}$. Then, $Q(n+1)$ is computed from

$$Q(n+1) = \operatorname{vec}^{-1} q(n+1) \in \mathbb{R}^{l_\theta \times (n_c(l_f + l_\theta)+1)}, \tag{39}$$

where vec^{-1} is the inverse operator, meaning $\operatorname{vec}^{-1}\operatorname{vec} Q(n) = Q(n)$. Also, Eqs. (35) and (36) are an RLS algorithm.

In summary, the RCA algorithm employed in the code-base consists of Eqs. (25), (33), and (35) through (39).

IV. Validation

The WRF model set up for validation employed three nested domains centered on the University of Kentucky flight field, which were defined within the WRF model to establish the geographic area of interest as shown in figure 3. On November 10, 2022, as part of UAV formation flight control testing at the flight field, u and v horizontal wind speed component data was incidentally gathered. Specifically, three UAVs – referred to as BC10B, BC10C, and BC10D – were simultaneously flown in a stacked leader-follower racetrack formation. The collected data was used in a 'batch update' validation approach as described below.

A. Batch Update Methodology

For the batch update validation approach, horizontal wind component data from UAVs BCB10C and BCB10D from 4 'clock' locations in a small racetrack flight pattern that occurred between 16:22:38 and 16:32:58 on 11 November 2022, was used as input for the RCA algorithm. This input data used a batch update procedure, meaning that the measurements were updated once per lap. The 3D flight patterns of the three UAVs used for the batch update approach and the four clock locations coinciding with positions of 3, 6, 9, and 12 o'clock are shown in Fig. 4 within the innermost nest, or

Domain 3. Data from UAV BC10B from these same four clock locations and time frames was used for validation. Note, as shown in Fig. 4, that the Domain 3 horizontal grid is composed of 16 WRF 'tiles', where a tile is a subsection of a WRF grid that is sent to a different processor for parallel computations. Thus, the geographic area covered by the three simultaneous flights is limited relative to the size of the modeled domain, as the vast majority of these flights are primarily in a single WRF 'tile'. Notwithstanding this limited geographic coverage, the data was deemed sufficient to utilize and provide a validation indicator.

The data was actually collected at a sample rate of 200 Hz. Therefore, to determine an observation at one of the four locations, measurements were averaged when the UAVs were within a 25 meters latitude and 25 meters longitude of said location. Thus, for all three UAVs, four averaged u and v observed values were established for each lap at an averaged timestamp and averaged altitude, with the latitude and longitude set to the associated i and j grid indices for the clock position on that lap.

The batch update procedure required that the four most recent u and v input observations from BC10C and BC10D be simultaneously updated. Consequently, a common timestamp was designated as when the second or laggard UAV crossed the 3 o'clock position in a given lap. Since the common timestamp did not exactly match the WRF model time steps, the RCA inputs were updated when the simulation time was more than or equal to the common timestamp. Also

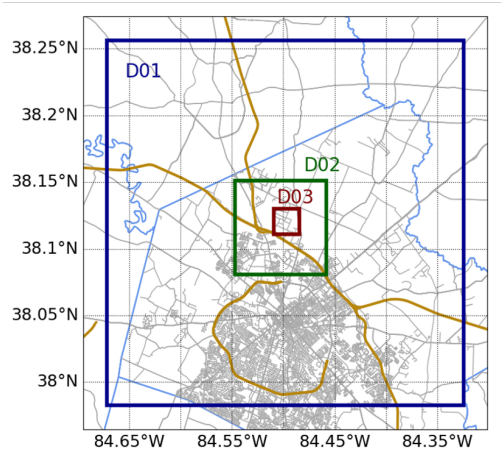

Fig. 3 Three nested domains centered on UK Flight Field

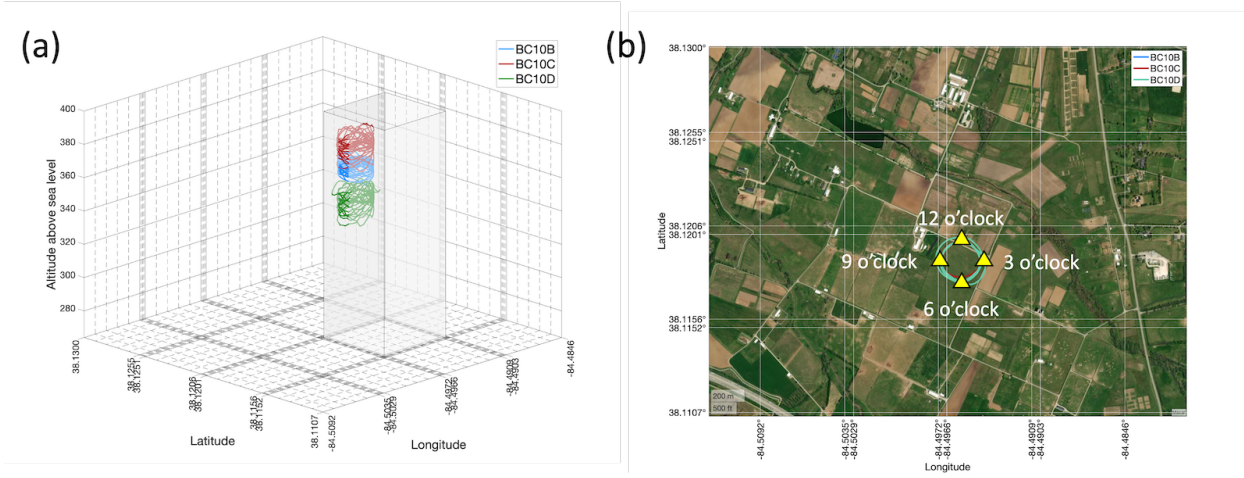

Fig. 4 Flight patterns of the three UAVs from 16:22:38 to 16:32:58 on 10 November 2022: (a) 3D plot where the x and y axes display the 16 WRF tiles within Domain 3, plus a 3D representation of the tile where the majority of the flight pattern occurred, and (b) 2D plot superimposed on a satellite map view also showing the 16 WRF tiles of Domain 3

note that given that the common timestamp was set at the 3 o'clock position, the measurements at the 12, 9, and 6 o'clock positions for the laggard UAV would be progressively latent or stale, while measurements for the faster or first UAV would be even more latent at each clock position. The advantage of the batch update approach is that the entire flow field is updated with the observations taken at roughly the same time – approximately within 30 seconds – with the same time stamp. Plus, the added benefit is that spatial variations for the RCA algorithm input data are precluded.

B. Model Setup

V. Model Setup

As previously stated, three nested domains were defined within the WRF model to establish the geographic area of interest centered on the University of Kentucky flight field, as previously shown in Fig. 3. All of the gray streets at the bottom of this figure show the city of Lexington, which is laid out in a hub and spoke configuration, while the dark yellow lines represent interstates or controlled access highways. Note that Domain 3 (D03) is the innermost domain. Other key setup information and run-time options are provided in Table 1.

Table 1 Key WRF inputs and set-up parameters

Parameter	Setting
WRF version	• 4.5
Nesting	• 3 two-way, nested domains (see Fig. 3)
Domain 3 geographic region	• Centered on the University of Kentucky flight field, just north of Lexington, KY
Domain 3 geographic area	• 4.72 km^2
Domain 3 horizontal grid resolution	• 50 m $\times$ 50 m • 45 $\times$ 45 grid indices • 16 WRF tiles (numbered 0 - 15)
Domain 3 vertical grid resolution	• 128 levels (`eta_levels`), with finer resolution lower in the atmosphere • Increasing from 50 m to 123 m up to an altitude of about 2,180 m • Above 2,180 m, increases from 440 m to 775 m up to the atmospheric top defined as a pressure of 5,000 Pa.
Initialization data	• National Centers for Environmental Prediction, Global Data Assimilation System, Final (NCEP GDAS/FNL) 0.25 Degree Global Tropospheric Analyses and Forecast Grids from NCAR [32]
Run simulation date/time	• 10 November 2022 from 16:00 to 16:49
Integration time steps	• 1 second for domains 1 and 3 • 1/3 of a second for domain 3
Physics option (`mp_physics`)	• 3, which is a simple and efficient WRF Single-Moment (WSM) scheme [18, 19]
LES option (`km_opt`)	• 2, which is a 1.5-order turbulent kinetic energy 3D closure scheme [18, 19]

Of notable importance is the Domain 3 horizontal grid size of 50 m $\times$ 50 m to enable precision meteorological forecasts. The vertical grid resolution was finer near the planetary surface and progressively became more coarse at upper atmospheric levels since UAV operations and contaminant clouds are typically located at lower atmospheric levels. Also, the LES option was enabled to enhance PBL modeling employing a 1.5-order turbulent kinetic energy scheme.

A. Validation Results

Two cases of the code were executed to allow for comparison and validation: 1) without the use of the RCA algorithm, referred to as the baseline case; and 2) with the use of the RCA algorithm, referred to as the adapted simulation case. The first validation step is to assess how the WRF-simulated flow field has changed as a result of the adaptation. Fig. 5 displays the baseline and RCA simulated 10-m wind speed and wind direction as a time progression composed of three individual snapshots. The various colors represent the 10-m wind speed magnitudes, while the wind barbs serve to indicate the wind direction. Figs. 5a, b, and c are progressive snapshots in time at 16:23:30, 16:30:00, and 16:33:00 on 11 November 2022, respectively, for the baseline case, while 5d, e, and f, respectively, are the same time snapshots for

the adapted simulation case. The location of the University of Kentucky flight field is notated as a star in the plots.

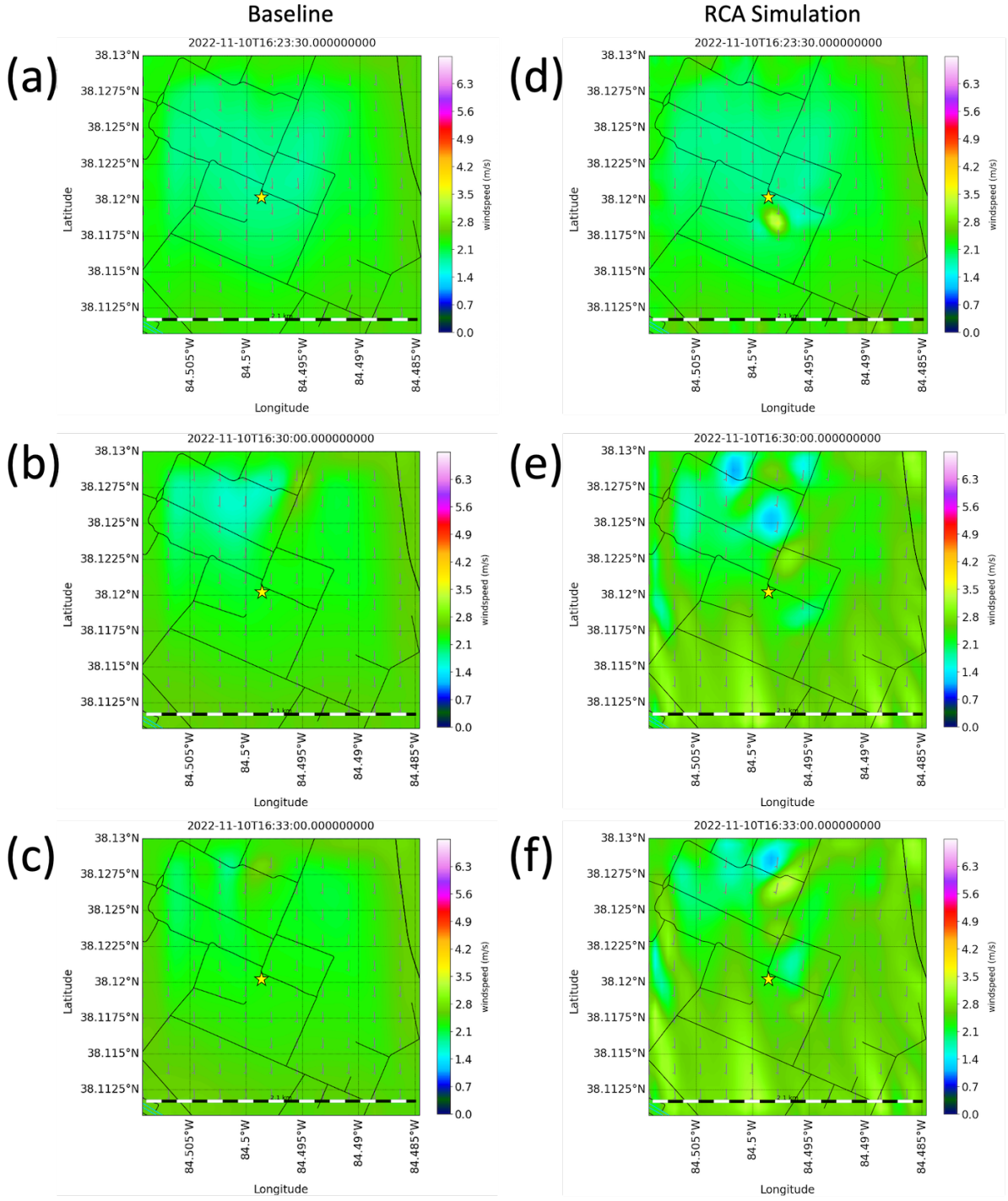

Fig. 5 Time progression of 10-m wind speed magnitudes and wind directions on 11 November 2022 for the batch update validation approach: (a) snapshot at time 16:23:30 for the baseline case; (b) snapshot at time 16:30:00 for baseline case; (c) snapshot at time 16:33:00 for the baseline case; (d) snapshot at time 16:23:30 for the RCA simulation case; (e) snapshot at time 16:30:00 for the RCA simulation case; (f) snapshot at time 16:33 for the RCA simulation case

A review of the baseline plots reveals that at 16:23:30, a zone of slightly lower wind speed is situated at and north of

the flying field. This region drifts further north around 16:30:00, and by 16:33:00, it essentially dissipates from east to west. While evaluation of the adapted simulation plots shows for the adapted horizontal wind speed components, just south of the flight field, a small circular zone of higher wind speed commences, as highlighted in yellow at 16:23:30. This lower wind speed region then advects with the overall flow regime towards the north before eventually fading, but induces two circular areas of lower wind speed shown in blue. In addition, at 16:30:00, a new circular area of higher wind speed develops, which then grows slightly and advects northward by 16:33:00. Furthermore, there are areas of higher wind speeds, yellow and yellowish-green colors, that are visible mostly in the lower portion of the RCA simulation charts but extend towards the north over time given the overall flow direction. Also, compared to the baseline, which is effectively a northerly wind, the adapted simulation wind direction on the eastern half of the domain is shifted to the north-northeast. These results indicate that the application of the RCA algorithm, utilizing flow field observations, does indeed have an effect on the WRF model output. The flow in the entire domain was affected even though only a small geographic region, primarily within a single WRF tile, was adapted. Moreover, adapting the flow to horizontal wind speed component observations produces changes vertically as well, since the simulated 10-m wind speeds are affected while the UAVS were broadly flown at altitudes between 300 m and 380 m.

The vertical changes in wind speeds due to adaptation are more readily visible in a vertical cross section of the flow. So, Figs. 6 and 7 display 1000-meter vertical cross sections at a constant latitude of 38.1201° and a constant longitude of -84.4977°, respectively. These figures are a time progression with the same snapshot times as the 10-m wind speed and wind direction figure. The wind speed is roughly 3 m/s in the baseline case for both the constant latitude and constant longitude vertical cross sections. Albeit, there are very small regions of lower wind speed at the PBL.

However, for the adapted simulation case, as soon as the adaptation starts, there is a clearly visible horizontal and vertical effect in both of the figures, as shown at 16:23:30. The vertical cross-section at constant latitude, Fig. 6d, particularly shows the initiation of the adaptation with a circular region of higher flow, shown in yellow between 390 m and 460 m, which also appears to induce a region of slower flow at the PBL, shown in blue. The area of higher flow, which coincides with the location of the observations used by the RCA algorithm, grows in strength and size and then basically persists, at slightly varying magnitudes and varying size, for the entire duration of the adaptation time progression. Interestingly, other regions of roughly circular higher wind speeds, as depicted in a yellow color, also form at varying locations and altitudes in these plots. For the adapted simulation in the vertical cross-section at constant longitude charts, Fig. 6, the same formation of the circular region of higher wind speed forms at the location of the UAV measurements between 38.1179° and 38.1193° latitude. This effect is visible as a very small yellow and red area near the PBL at 16:23:30 and a larger but faint yellow area between 390 and 460 m altitude at the same latitudes at 16:30:00. This region grows in size and magnitude and advects north along with the overall flow, as seen at 16:33:00. This formation of a region of higher wind speed and advection to the north occurs repeatedly during the adaptation time frame. Therefore, based on Figs. 5, 6, and 7, the RCA algorithm does cause changes in the overall WRF simulated flow field.

The second and key validation check is to assess the adapted WRF simulation to the BC10B observations, since the data collected by this UAV was not used to feed the RCA algorithm. These comparisons, along with the baseline, are shown in Figs.8 and 9 for the u and the υ wind speed components, respectively. In addition, Fig. 10 breaks down the u and the υ BC10B measurements compared to the adapted WRF simulation at the four clock positions.

In terms of the overall u and υ charts, compared to the baseline, the adapted simulation better represents the variation in the horizontal wind speed components. However, the adapted value magnitudes are generally not as high nor as low as the measurements. The υ simulation values visually appear to better follow the pattern of the BC10B measurements over time relative to the u values, particularly since there are large differences around 16:24:20, between 16:25:48 and 16:26:42, and between 16:28:30 and 16:29:24.

A visual evaluation of the horizontal wind speed component comparisons at the four clock positions shows that the adapted simulation follows the general measurement trend. Specifically, the u values are basically flat over time at all four locations, while the υ values are slightly increasing over time, although there is variation in both wind speed components within these broad trends. Additionally, the baseline case results also have these same trends for u and υ but are linear over time.

Importantly, in terms of accuracy improvement, Table 2 displays the average absolute errors and percentage reductions of the baseline and adapted simulation relative to the BC10B measurements for the four clock locations, as well as overall. Interestingly, the adapted simulation's υ absolute errors actually get respectively worse by 7.7% and 17.1% than the baseline at the 6 and 9 o'clock positions. Note that these are displayed as negative values in terms of percentage "reduction". Also, at 3 o'clock, the adapted simulation's u average absolute error is marginally worse than the baseline by 1.0%. Only for the 12 o'clock position is the adapted simulation's average absolute error less than the

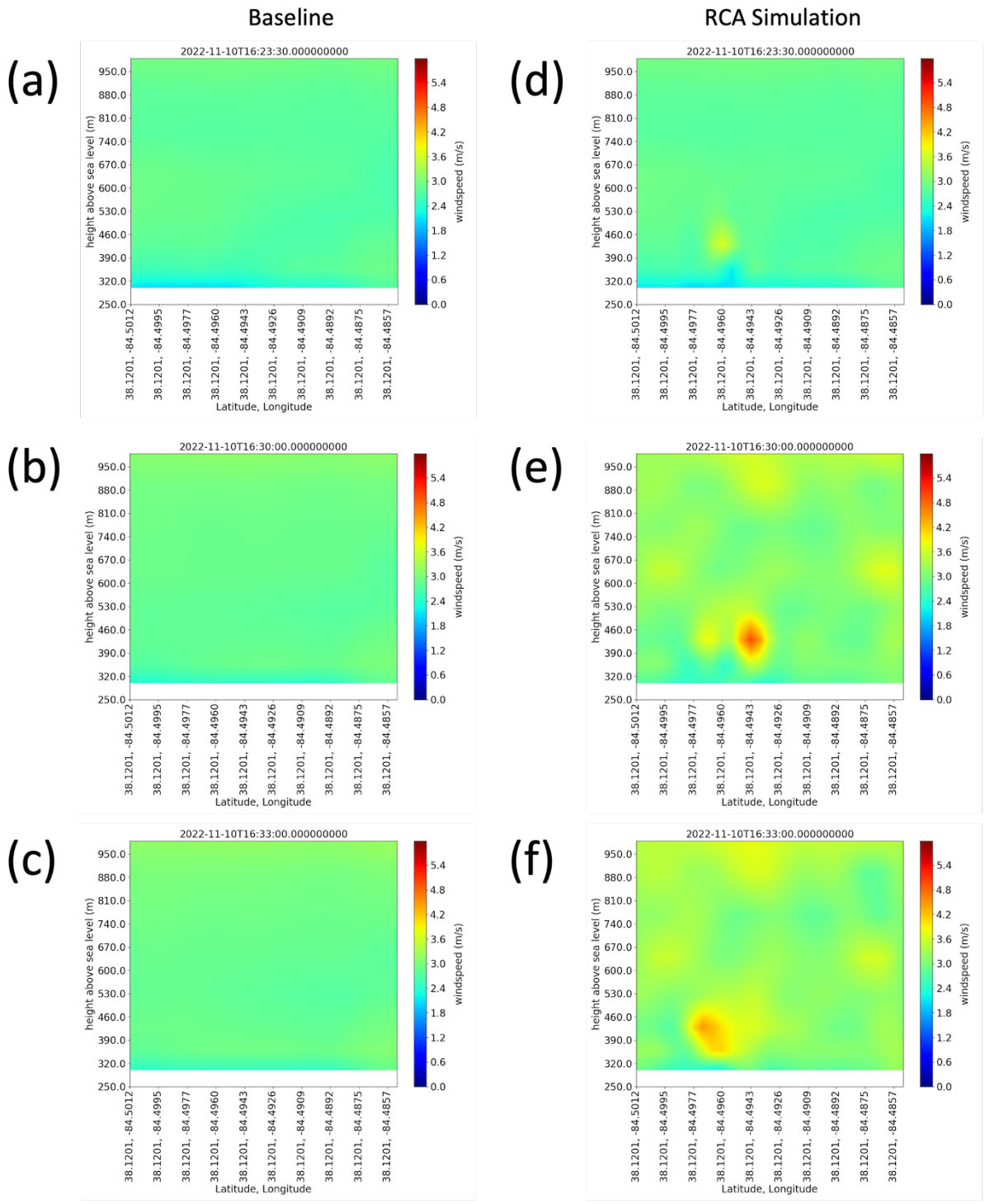

Fig. 6 Time progression for 1000-meter vertical cross-section wind speed magnitudes at a constant latitude of 38.1201° on 11 November 2022, for the batch update validation approach: (a) snapshot at time 16:25 for baseline case; (b) snapshot at time 16:30 for baseline case; (c) snapshot at time 16:33 for baseline case; (d) snapshot at time 16:25 for RCA simulation case; (e) snapshot at time 16:30 for RCA simulation case; (f) snapshot at time 16:33 for RCA simulation case

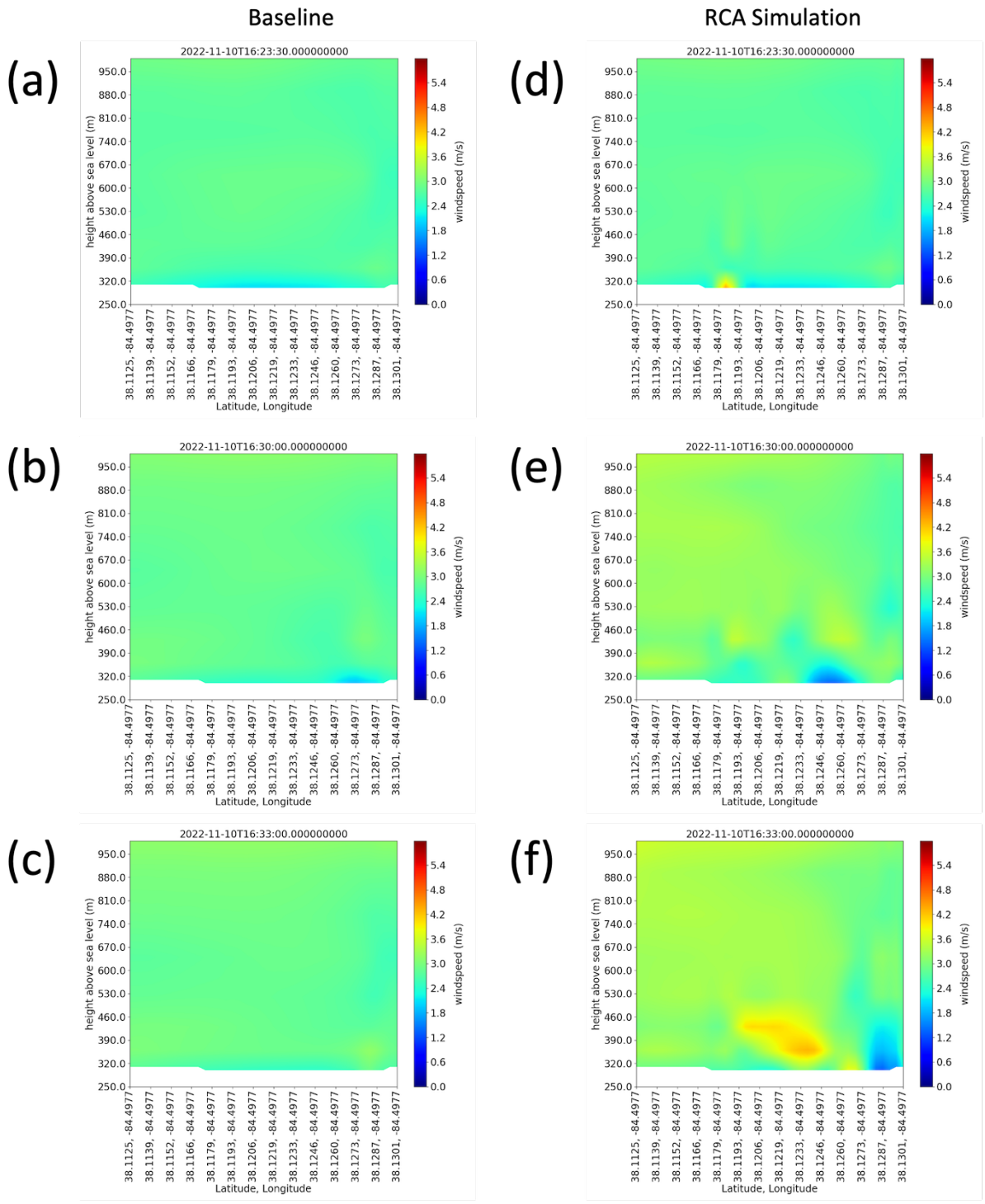

Fig. 7 Time progression for 1000-meter vertical cross-section wind speed magnitudes at a constant longitude of -84.4977° on 11 November 2022, for the batch update validation approach: (a) snapshot at time 16:25 for baseline case; (b) snapshot at time 16:30 for baseline case; (c) snapshot at time 16:33 for baseline case; (d) snapshot at time 16:25 for RCA simulation case; (e) snapshot at time 16:30 for RCA simulation case; (f) snapshot at time 16:33 for RCA simulation case

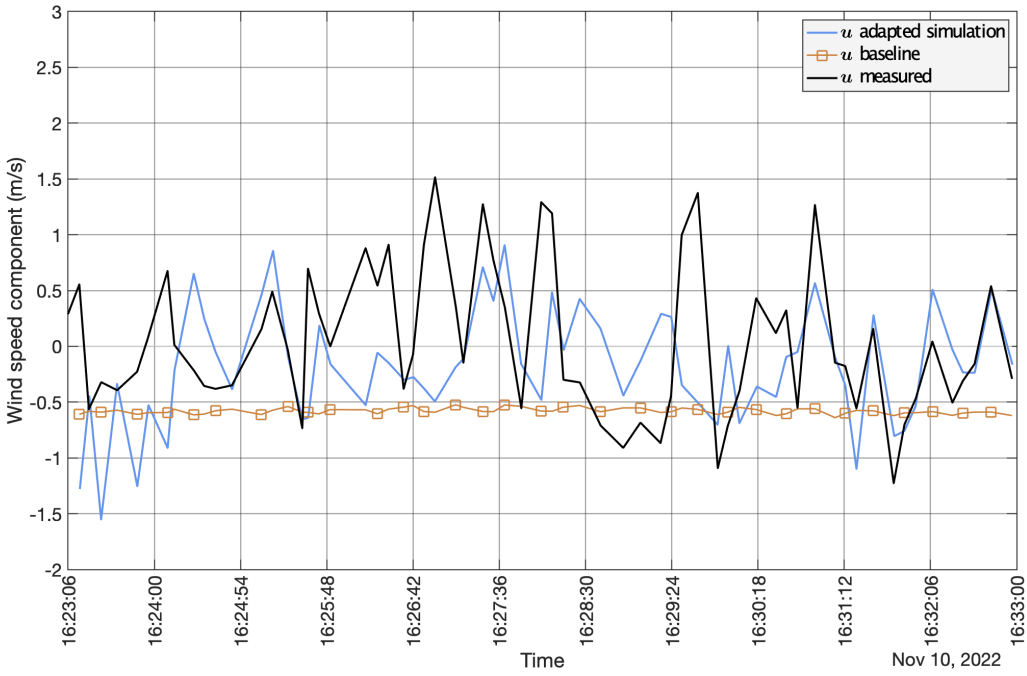

Fig. 8 Comparison of the WRF-adapted simulation to the BC10B measured u wind speed component over time for the batch update validation approach

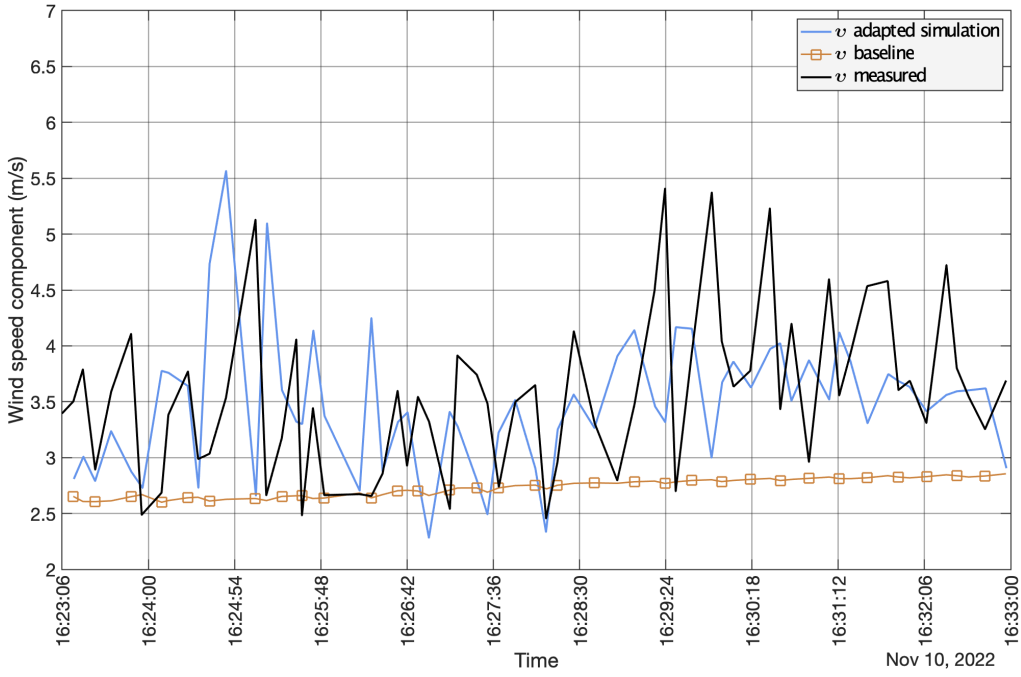

Fig. 9 Comparison of the WRF-adapted simulation to the BC10B measured v wind speed component over time for the batch update validation approach

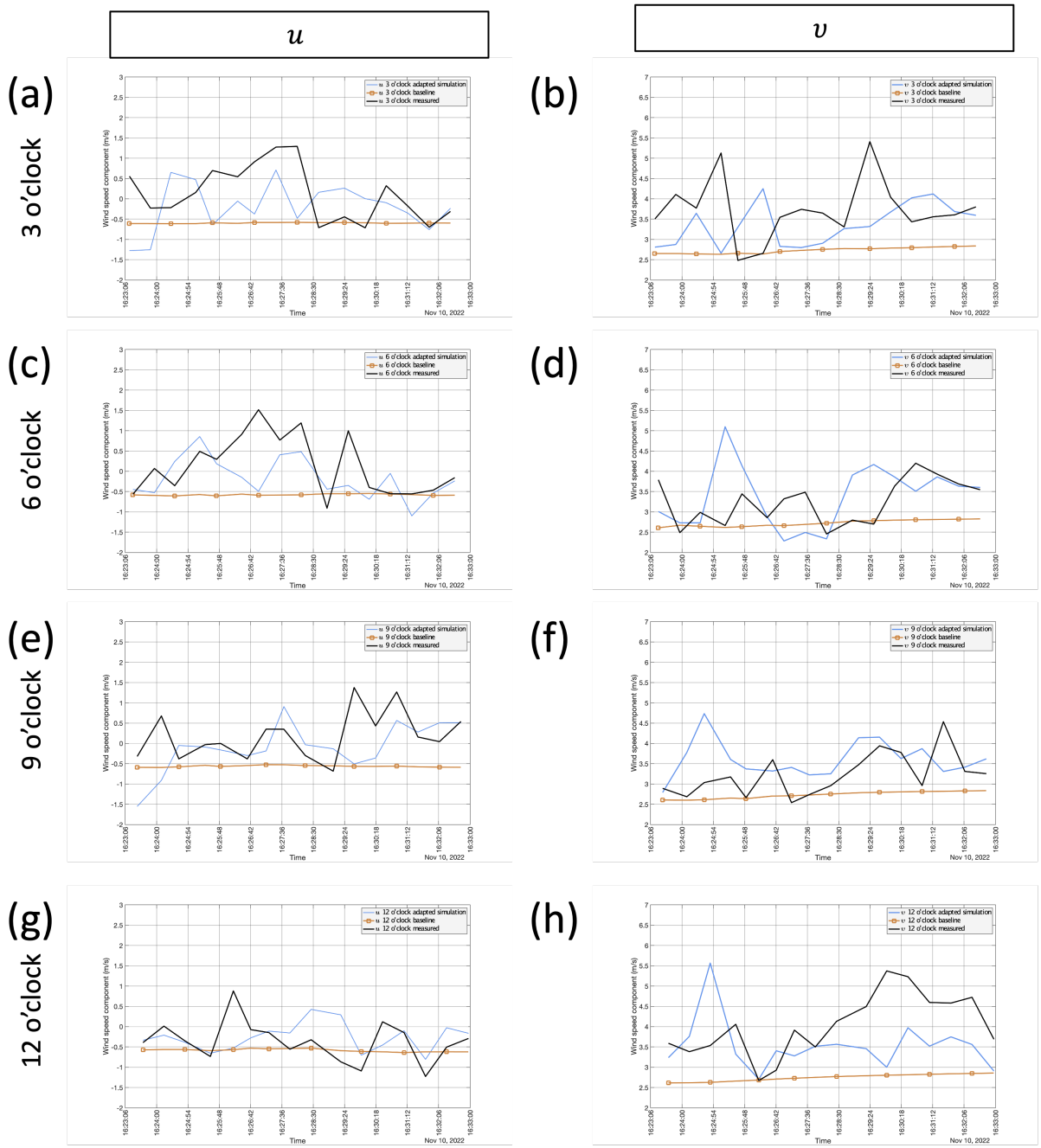

Fig. 10 Comparison of BC10C measured, baseline, and adapted simulation horizontal wind speed components at four fixed clock locations over time: (a) u comparison at 3 o'clock; (b) v comparison at 3 o'clock; (c) u comparison at 6 o'clock; (d) v comparison at 6 o'clock; (e) u comparison at 9 o'clock; (f) v comparison at 9 o'clock; (g) u comparison at 12 o'clock; (h) v comparison at 12 o'clock

baseline for both u and v, even though the 3 o'clock position had the least stale measurements, as described in the batch update approach (Section **??**). Therefore, in this case, there does not appear to be a discernible inverse correlation between data latency and adapted simulation results, since a better result was achieved in a clock location with higher latency.

Overall, however, for the adapted simulation, both horizontal wind speed component average absolute errors are reduced by the same amount of 14.2% when compared to the baseline. Therefore, this result, when combined with the

Table 2 Batch update u and υ mean absolute error breakdown for the four measurement clock positions

Clock location	Wind speed component	Mean absolute error (m/s)		Reduction percentage
		Baseline	Adapted simulation	
3 o'clock	u	0.78149	0.78953	-1.0%
	υ	1.02671	0.82991	19.2%
6 o'clock	u	0.76551	0.57640	24.7%
	υ	0.59483	0.64058	-7.7%
9 o'clock	u	0.77243	0.58447	24.3%
	υ	0.51174	0.59923	-17.1%
12 o'clock	u	0.41745	0.39887	4.5%
	υ	1.28074	0.85939	32.9%
All	u	0.68422	0.58732	14.2%
	υ	0.85351	0.73227	14.2%

more representative horizontal wind speed component variation patterns of the adapted simulation, indicates that the RCA algorithm can improve the WRF model output with batch data updates. Finally, note that this improvement in the simulation accuracy was achieved with very little observational data coverage of the geographic/atmospheric area under examination.

VI. Conclusions

This study examined the viability of a means to improve precision weather forecasting via the use of the WRF model augmented with the RCA algorithm. While the ultimate operational concept is to achieve a DART solution, the scope of this effort was focused on developing a data-driven, adaptive solution while being mindful of the real-time requirement. The augmented WRF model was validated using incidental u and υ data collected from three UAVs during a flight formation flight test on 10 November 2022. Based on the results of the analyses, the following conclusions can be drawn:

- The RCA algorithm will work properly with the WRF model, plus the adaptation not only changes the simulated u and υ values at the observed location, but it also affects these values for the entire geographic/atmospheric area modeled.
- The RCA algorithm improved the overall accuracy of the WRF forecast, as the mean absolute errors of the adapted simulation were less than the baseline WRF model by 14.2% for both u and υ. However, the adapted simulation was less accurate than the baseline at the 3 o'clock location for the u mean absolute error and at the 6 and 9 o'clock positions for the υ mean absolute errors.
- The 14.2% mean absolute error reduction may understate potential real-time results since the geographic/atmospheric coverage of the RCA algorithm input measurements was limited and primarily within a single WRF tile. However, even with this limited coverage of the simulated region, the entire flow field was affected.
- Further testing is needed to both further validate the model and to examine the impact of adapting additional meteorological parameters, such as pressure, temperature, and relative humidity.

VII. Future Work Plans

Flight tests were conducted in August 20023 at the University of Kentucky flight field, designed specifically to validate the WRF moodel augmented with the RCA algorithm. Four flight tests were performed on two different days using four UAVS flying in four separate racetracks, covering each WRF tile in Domain 3. The data has recently been made available. Therefore, the immediate next step is to further validate the model and evaluate the impact of adapting other meteorological parameters.

Ultimately, once a minimal viable product (MVP) or full system solution is developed, the viability of a real-time or

near-real-time solution for the operational concept can be assessed and validated.

Acknowledgments

Financial support for this work was provided by the National Science Foundation (CNS-1932105). The authors would also like to thank the University of Kentucky Center for Computational Sciences and Information Technology Services Research Computing for their support and use of the Lipscomb Compute Cluster and associated research computing resources.

References

[1] "Commercial Drone Market, 2023-2030," Tech. Rep. FBI102171, Fortune Business Insights, May 2023. URL https://www.fortunebusinessinsights.com/commercial-drone-market-102171, last checked November 3, 2023.

[2] "Commercial Drone Market, Forecast 2021-2030," Tech. Rep. 66633301, Strategic Market Research, December 2022. URL https://www.strategicmarketresearch.com/market-report/commercial-drones-market, last checked November 3, 2023.

[3] Cohn, P., Green, A., Langstaff, M., and Roller, M., "Commercial drones are here: The future of unmanned aerial systems," Article, McKinsey and Company, December 2017. URL https://www.mckinsey.com/industries/travel-logistics-and-infrastructure/our-insights/commercial-drones-are-here-the-future-of-unmanned-aerial-systems, last checked November 3, 2023.

[4] "Military Drone Market, 2023-2030," Tech. Rep. FBI102181, Fortune Business Insights, June 2023. URL https://www.fortunebusinessinsights.com/military-drone-market-102181, last checked November 3, 2023.

[5] Ergene, Y., "Analysis of Unmanned Systems in Military Logistics," Master's thesis, Naval Postgraduate School, December 2016. URL https://www.hsdl.org/?view&did=810945, last checked November 3, 2023.

[6] "Yearly Summary Report Database - Incidents by Result," Webpage, March 2023. URL www.phmsa.dot.gov/hazmat-program-management-data-and-statistics/data-operations/incident-statistics, last checked November 3, 2023.

[7] Blum, A., *The Weather Machine: A Journey Inside the Forecast*, Harper Collins Publishers, New York, 2019.

[8] Mayer, S., "Application and Improvement of the Unmanned Aerial System SUMO for atmospheric boundary layer studies," Master's thesis, University of Bergen, Norway, June 2011. URL https://www.uib.no/filearchive/phd_mayer.pdf, last checked November 3, 2023.

[9] Passner, J. E., Kirby, S., and Jameson, T., "Using Real-Time Weather Data from an Unmanned Aircraft System to Support the Advanced Research Version of the Weather Research and Forecast Model," Tech. Rep. ARL-TR-5950, Army Research Laboratory, April 2012. URL https://apps.dtic.mil/dtic/tr/fulltext/u2/a561959, last checked November 3, 2023.

[10] Jacob, J. D., Chilson, P. B., Houston, A. L., and Smith, S. W., "Considerations for Atmospheric Measurements with Small Unmanned Aircraft Systems," *Atmosphere*, Vol. 9, No. 7, 2018. https://doi.org/10.3390/atmos9070252, URL https://www.mdpi.com/2073-4433/9/7/252.

[11] Nolan, P. J., Pinto, J., González-Rocha, J., Jensen, A., Vezzi, C. N., Bailey, S. C. C., De Boer, G., Diehl, C., Laurence, R., Powers, C. W., Foroutan, H., Ross, S. D., and Schmale, D. G., "Coordinated Unmanned Aircraft System (UAS) and Ground-Based Weather Measurements to Predict Lagrangian Coherent Structures (LCSs)," *Sensors*, Vol. 18, No. 12, 2018. https://doi.org/10.3390/s18124448, URL https://www.mdpi.com/1424-8220/18/12/4448.

[12] Liu, Y., Liu, Y., Muñoz-Esparza, D., Hu, F., Yan, C., and Miao, S., "Simulation of Flow Fields in Complex Terrain with WRF-LES: Sensitivity Assessment of Different PBL Treatments," *Journal of Applied Meteorology and Climatology*, Vol. 59, No. 9, 2020, pp. 1481 – 1501. https://doi.org/10.1175/JAMC-D-19-0304.1, URL https://journals.ametsoc.org/view/journals/apme/59/9/jamcD190304.xml.

[13] Wiersema, D., "Mesoscale to Microscale Atmospheric Modeling Over Complex Terrain," Ph.D. thesis, UC Berkeley, 2020. URL https://escholarship.org/uc/item/5dk5564n, last checked November 3, 2023.

[14] Prieto-Herráez, D., Frías-Paredes, L., Cascón, J., Lagüela-López, S., Gastón-Romeo, M., Asensio-Sevilla, M., Martín-Nieto, I., Fernandes-Correia, P., Laiz-Alonso, P., Carrasco-Díaz, O., Sáez-Blázquez, C., Hernández, E., Ferragut-Canals, L., and González-Aguilera, D., "Local wind speed forecasting based on WRF-HDWind coupling," *Atmospheric Research*, Vol. 248, 2021, p. 105219. https://doi.org/https://doi.org/10.1016/j.atmosres.2020.105219, URL https://www.sciencedirect.com/science/article/pii/S0169809520311558.

[15] Abdelghaffar, H. M., Woolsey, C. A., and Rakha, H. A., "Comparison of Three Approaches to Atmospheric Source Localization," *Journal of Aerospace Information Systems*, Vol. 14, No. 1, 2017, pp. 40–52. https://doi.org/10.2514/1.I010440, URL https://doi.org/10.2514/1.I010440.

[16] Pinto, J. O., Jensen, A. A., Jiménez, P. A., Hertneky, T., Muñoz Esparza, D., Dumont, A., and Steiner, M., "Real-time WRF large-eddy simulations to support uncrewed aircraft system (UAS) flight planning and operations during 2018 LAPSE-RATE," *Earth System Science Data*, Vol. 13, No. 2, 2021, pp. 697–711. https://doi.org/10.5194/essd-13-697-2021, URL https://essd.copernicus.org/articles/13/697/2021/.

[17] Muñoz-Esparza, D., Shin, H. H., Sauer, J. A., Steiner, M., Hawbecker, P., Boehnert, J., Pinto, J. O., Kosović, B., and Sharman, R. D., "Efficient Graphics Processing Unit Modeling of Street-Scale Weather Effects in Support of Aerial Operations in the Urban Environment," *AGU Advances*, Vol. 2, No. 2, 2021, p. e2021AV000432. https://doi.org/10.1029/2021AV000432, URL https://agupubs.onlinelibrary.wiley.com/doi/abs/10.1029/2021AV000432, e2021AV000432 2021AV000432.

[18] Wang, W., Bruyère, C., Duda, M., Dudhia, J., Gill, D., Kavulich, M., Werner, K., Chen, M., Lin, H.-C., Michalakes, J., Rizvi, S., Zhang, X., Berner, J., Munoz-Esparza, D., Reen, B., Ha, S., and Fossell, K., "WRF User's Guide documentation Version 4.5.1," Online manual, National Center for Atmospheric Research (NCAR), July 2023. URL https://www2.mmm.ucar.edu/wrf/users/wrf_users_guide/build/html/index.html, last checked November 3, 2023.

[19] Skamarock, W. C., Klemp, J. B., Dudhia, J., Gill, D. O., Liu, Z., Berner, J., Wang, W., Powers, J. G., Duda, M. G., Barker, D., and Huang, X.-Y., "A Description of the Advanced Research WRF Model Version 4.3," NCAR Technical Notes NCAR/TN-556+STR, NCAR UCAR, 2021. https://doi.org/10.5065/1dfh-6p97.

[20] Rai, K., Berg, L., Kosovic, B., Mirocha, J., Pekour, M., and Shaw, W., "Comparison of Measured and Numerically Simulated Turbulence Statistics in a Convective Boundary Layer Over Complex Terrain," *Boundary-Layer Meteorology*, Vol. 163, 2017, pp. 69–89. https://doi.org/10.1007/s10546-016-0217-y.

[21] Liu, Y., Warner, T., Liu, Y., Vincent, C., Wu, W., Mahoney, B., Swerdlin, S., Parks, K., and Boehnert, J., "Simultaneous nested modeling from the synoptic scale to the LES scale for wind energy applications," *Journal of Wind Engineering and Industrial Aerodynamics*, Vol. 99, No. 4, 2011, pp. 308–319. https://doi.org/10.1016/j.jweia.2011.01.013.

[22] Udina, M., Montornés, À., Casso, P., Kosović, B., and Bech, J., "WRF-LES Simulation of the Boundary Layer Turbulent Processes during the BLLAST Campaign," *Atmosphere*, Vol. 11, No. 11, 2020. https://doi.org/10.3390/atmos11111149.

[23] Laprise, R., "The Euler Equations of Motion with Hydrostatic Pressure as an Independent Variable," *Monthly Weather Review*, Vol. 120, No. 1, 1992, pp. 197–207. https://doi.org/10.1175/1520-0493(1992)120<0197:TEEOMW>2.0.CO;2.

[24] Park, S.-H., Skamarock, W. C., Klemp, J. B., Fowler, L. D., and Duda, M. G., "Evaluation of Global Atmospheric Solvers Using Extensions of the Jablonowski and Williamson Baroclinic Wave Test Case," *Monthly Weather Review*, Vol. 141, No. 9, 2013, pp. 3116–3129. https://doi.org/10.1175/MWR-D-12-00096.1.

[25] Li, Z., Zhang, H., Bailey, S. C. C., Hoagg, J. B., and Martin, A., "A data-driven adaptive Reynolds-averaged Navier–Stokes k-ω model for turbulent flow," *Journal of Computational Physics*, Vol. 345, 2017, pp. 111–131. https://doi.org/10.1016/j.jcp.2017.05.009.

[26] Li, Z., Hoagg, J. B., Martin, A., and Bailey, S. C., "Retrospective cost adaptive Reynolds-averaged Navier–Stokes k-ω model for data-driven unsteady turbulent simulations," *Journal of Computational Physics*, Vol. 357, 2018, pp. 353–374. https://doi.org/10.1016/j.jcp.2017.11.037.

[27] Fu, R., Sinha, S., Barrow, C., Maddox, J. F., Hoagg, J. B., and Martin, A., "A Data-Driven Approach For Real-Time Estimation of Material Uncertainty," *AIAA Aviation 2022 Forum*, Chicago, IL, 2022. https://doi.org/10.2514/6.2022-3728.

[28] Sinha, S., Fu, R., Bailey, S. C., Hoagg, J. B., and Martin, A., "Precision Meteorological Prediction Employing A Data-Driven, Adaptive, Real-Time (DART) Approach," *Aerospace Europe Conference 2023* 10^{th} *EUCASS* - 9^{th} *CEAS*, Lausanne, CH, 2023. https://doi.org/10.13009/EUCASS2023-836.

[29] Venugopal, R., and Bernstein, D., "Adaptive disturbance rejection using ARMARKOV/Toeplitz models," *IEEE Transactions on Control Systems Technology*, Vol. 8, No. 2, 2000, pp. 257–269. https://doi.org/10.1109/87.826797.

[30] Hoagg, J., and Bernstein, D., "Cumulative retrospective cost adaptive control with RLS-based optimization," *Proceedings of the 2010 American Control Conference, ACC 2010*, 2010, pp. 4016 – 4021. https://doi.org/10.1109/ACC.2010.5530434.

[31] Hoagg, J. B., and Bernstein, D. S., "Retrospective Cost Model Reference Adaptive Control for Nonminimum-Phase Systems," *Journal of Guidance, Control, and Dynamics*, Vol. 35, No. 6, 2012, pp. 1767–1786. https://doi.org/10.2514/1.57001.

[32] National Centers for Environmental Prediction, National Weather Service, NOAA, U.S. Department of Commerce, "NCEP GDAS/FNL 0.25 Degree Global Tropospheric Analyses and Forecast Grids," Online Dataset, 2015. https://doi.org/10.5065/D65Q4T4Z.